Available online at www.sciencedirect.com

jmr&t Journal of Materials Research and Technology

journal homepage: www.elsevier.com/locate/jmrt

Original Article

Improving thermal conductivity of a nickel-based alloy through advanced electromagnetic coupling treatment

Qianwen Zhang [a,b], Xiaotong Wang [a,b], Yi Qin [c], Gening He [d], Shiyuan Zhang [a,b], Kunlan Huang [a,b,*], Jie Wang [a,b]

[a] School of Mechanical Engineering, Sichuan University, Chengdu 610065, PR China
[b] Yibin Institute of Industrial Technology, Sichuan University Yibin Park, Yibin 644000, PR China
[c] Centre for Precision Manufacturing, DMEM, The University of Strathclyde, James Weir Building, 75 Montrose Street, Glasgow G1 1XJ, UK
[d] Nuclear Power Institute of China, Chengdu 610200, PR China

ARTICLE INFO

Article history:
Received 20 September 2022
Accepted 10 November 2022
Available online 17 November 2022

Keywords:
Superalloys
Electromagnetic coupling treatment
Thermal conductivity
Dislocations
Solute atoms

ABSTRACT

In this study, in response to the requirement for a higher heat transfer efficiency of the small-scale nuclear power reactors, a novel material treatment method in the form of electromagnetic coupling treatments (EMCT) was studied and applied to improve the thermal properties of a nickel-based austenitic alloy - Alloy 690, often used for the heat transfer tube of the steam generator. The effect of the EMCT on the thermal properties of Alloy 690 was investigated and the evolution of microstructure and texture under the influences of the electromagnetic coupling field was studied. These were compared with that produced by the treatments with electric field only and magnetic field only respectively. The results showed that the thermal conductivity of Alloy 690 could be improved by 17.5% by the EMCT approach. The further study revealed that the migration and annihilation of dislocations and the precipitation of the $M_{23}C_6$ phase are the key factors influencing the changes of the thermal conductivity, and the magnetoplastic and electroplastic effects provide the impetus to the evolution of the microstructure. The proposed and proven electromagnetic coupling treatment technology provides a novel method for improving the thermal conductivity of nickel-based superalloys and the study provides an important technical guidance to the design and research of critical nickel-based alloy components, such as that used in small-scale nuclear power reactors. At the same time, the work reported in this paper demonstrates a new approach that could also be used for the study of the thermal properties of other superalloys.

* Corresponding author.
E-mail address: huangkunlan@scu.edu.cn (K. Huang).

https://doi.org/10.1016/j.jmrt.2022.11.066

1. Introduction

Alloy 690 is a nickel-based austenitic alloy developed from Alloy 600 by increasing chromium and reducing carbon. It is widely used in the aerospace, chemical, and nuclear power generation industries due to its excellent corrosion resistance and formability. As the key component of a pressurized water reactor (PWR) steam generator (SG), most of the heat transfer tubes are currently made of Alloy 690. The heat transfer tubes need to have two main characteristics in engineering applications: safety and functionality.

The main factor affecting the safety of SG heat transfer tubes is the corrosion damage. As the working environment of the SG heat transfer tube is severe, the material of the heat transfer tube must have the ability to resist uniform corrosion and stress corrosion fracture. The main factor affecting its functionality is heat transfer efficiency. The improvement of heat transfer efficiency brought by the improvement of thermal conductivity can reduce the uneven distribution of the temperature gradient of the heat transfer tube. This will reduce the occurrence of stress corrosion caused by heat-induced stress, prolong the service life of the heat transfer tube [1], and create higher economic benefits. Improving heat transfer efficiency is in line with the trend in new nuclear power plant technology for higher energy utilization and longer service life. This research is particularly significant for the development of small advanced modular multipurpose reactors.

Presently, the actual heat transfer efficiency of the heat transfer tube in use is about 80% of the design value. The thermal conductivity of the alloy is mainly controlled by the composition of the alloy, lattice distortion, intragranular and grain boundary (GB) defects, etc. The thermal conductivity is sensitive to the microstructure and fluctuates with microstructural changes. Although the corrosion resistance of Alloy 690 is improved by increasing Cr content, the addition of alloy elements will inevitably cause a large distortion of the alloy lattice, increase the number of solid atoms in the matrix, and enhance the scattering effect of solute atoms on electrons and phonons. As a result, the thermal conductivity of Alloy 690 (13.5 $W\ m^{-1}\ K^{-1}$ at 100 °C) is relatively lower than that of Alloy 600 (15.9 $W\ m^{-1}\ K^{-1}$ at 100 °C). Particularly, when Mg–Zn alloys are within the maximum solubility of Zn, the addition of Zr can reduce the solubility of Zn in the α-Mg matrix, weaken the lattice distortion and improve the thermal conductivity [2,3].

The change in grain size affects the thermal conductivity of the alloy. Fine-grain size and a large total area of the GBs contribute to lower thermal conductivity. GB is a special surface defect with a large number of dislocation defects nearby. These defects will scatter free electrons and phonons, reduce the average free path of electrons and phonons, and reduce the thermal conductivity of the alloy [4]. The thermal conductivity of Mg–Zn alloy and Mg–Al alloy is lower than that of the as-cast alloy after extrusion treatment [5–8], which is due to the dynamic recrystallization of the alloy during extrusion. A large number of annealing twins are produced in Alloy 690 during thermal deformation and heat treatment. Similar to GBs and subgrain boundaries, the twin boundaries will also affect the thermal conductivity of the alloy.

$M_{23}C_6$ carbides precipitated during the aging process of Alloy 690, resulting in the corresponding distortion of the alloy lattice. Rudajevová, A [1,4,9–11] et al. have researched the thermal properties of Mg–Al alloy. The research shows that the addition of Si atoms after solid solution treatment will inhibit the precipitation of $Mg_{17}Al_{12}$ and increase the content of heterogeneous solute Al atoms in the matrix. The scattering of phonons and electrons by solute atoms is enhanced, and the thermal conductivity of the alloy is reduced.

Electromagnetic coupling treatment (EMCT) is a technology that uses an energy field to modify the microstructure and regulate the properties of magnetic materials. The electric current introduced by the electric field increases the atomic kinetic energy in the material which can affect the dislocation movement. A magnetostrictive effect will occur in ferromagnetic materials in a magnetic field, this will cause a change in dislocation structure and change the distribution, arrangement, and migration of atoms. EMCT offers advantages over single physical field treatment [12,13] and provides a unique opportunity for regulating the thermal conductivity of nickel-based alloys.

Presently, the research on nickel-based alloy materials mostly focuses on corrosion resistance rather than thermal properties. Existing methods to regulate the thermal conductivity of nickel-based alloys mainly include solid solution treatment, heat treatment, and other traditional methods. Therefore, the effect of EMCT on the thermal conductivity of Alloy 690 was investigated. The Alloy 690 heat transfer tubes were treated with an EMCT device independently developed and designed. The thermal conductivity, thermal diffusivity, specific heat capacity, and electrical conductivity were measured to evaluate the effect of EMCT on the thermal properties of Alloy 690.

The microstructure evolution of Alloy 690 was characterized by scanning electron microscope (SEM), transmission electron microscope (TEM), and electron back-scatter diffraction (EBSD) quantitative phase analysis. The changes in microstructure and properties after the EMCT were evaluated. This research hopes to provide direction and theoretical reference for the remanufacturing process of nickel-based or iron nickel-based alloys.

2. Materials and methods

2.1. Materials

The experimental materials of this study were Alloy 690 heat transfer tubes with a dimension of Φ 17.48 mm (external diameter) × 1.02 mm (thickness) × 500 mm (height). The manufacturing processes of as-received heat transfer tubes were vacuum induction furnace melting, forging, hot extrusion, hot rolling, cold rolling, and heat treatment. Test specimens were cut from the heat transfer tubes for electromagnetic coupling treatment. The chemical composition and physical constant of the tested Alloy 690 are given in Table 1 and Table 2, respectively.

Table 1 – Chemical composition (wt. %) of the Alloy 690 tubes.

Element	Cr	Fe	Cu	C	Co	Ti	Al	Mn	Si	P	S	Ni
Wt.%	29.77	9.81	0.12	0.02	0.05	0.2	0.2	0.2	0.05	0.01	0.01	Bal

2.2. Electromagnetic coupling treatment experiments

The EMCT experiments were conducted using an EMCT experiment platform independently designed and customized by Sichuan University (Chengdu, China). The EMCT experiment platform is mainly composed of an electric and magnetic field generating unit and a coupling execution unit, as shown in Fig. 1. The electric field generating unit converts 380 V/50 Hz industrial AC into DC with a maximum current of 5000 A and a voltage range of 0–10 V through the electric field generating power supply. The copper electrode is connected to the electric field generating a power supply as the output of the electric field. The magnetic field generating unit is mainly composed of a magnetic field generating power supply and a solenoid. The capacitor bank of the magnetic field generating power supply discharges instantaneously after energy storage. The solenoid is composed of multiple ring coils. When a large current pass through the solenoid, the magnetic field generated by each ring coil is vector superimposed. The magnetic field intensity and frequency are regulated by controlling the charge saturation and discharge beat of the capacitor bank. The space inside the solenoid forms a cavity filled with the magnetic field. The magnetic field intensity is unevenly distributed in the cavity with the highest intensity at the center. The EMCT experiment platform can generate a magnetic field with an intensity of 0–3.5 T and a frequency of 1–100 Hz. The field coupling executive unit is composed of an executive driving mechanism and a PLC control system. The executive driving mechanism holds the specimen to be treated and connects it to the center of the magnetic field and electric field. The PLC system connects the power supply for the electric and magnetic fields and controls the synchronous output of these fields through programming to complete the EMCT experiments. The whole process was carried out at room temperature and standard atmospheric pressure. The EMCT experimental parameters of test specimens in this study are shown in Table 3. The electric field frequency and the magnetic field frequency are both 50 Hz, and the processing time is 250 s.

Table 2 – Physical constants of the Alloy 690 tubes [14].

Physical properties	Value
Density (g/cm^3)	8.13
Specific heat (J·kg^{-1}·K^{-1})	471
Yield strength (Mpa)	276–345
Electric resistivity at 100 °C (10^{-8} Ω m)	116
Thermal conductivity at 100 °C (W m^{-1}·K^{-1})	13.5
Elastic modulus (GPa)	211
Poisson's ratio	0.289
Melting temperature range (°C)	1343–1377
Permeability at 200 Oe (H/m)	1.001
Tensile strength (MPa)	≥586

2.3. Thermal performance test

The thermal diffusivity and thermal conductivity of the test specimens were determined by laser flash analysis (LFA 467 HyperFlash) according to ASTM E1461-13. The test specimen was a thin disc of Φ 17.48 mm × 1.02 mm. Before the test, a graphite coating was evenly sprayed on both sides of the specimen. To simulate the thermal conductivity under the actual working conditions, the test environment is an argon atmosphere at 300 °C. The thermal diffusion coefficient can be calculated by the following equation:

$$\alpha = 0.13879 \times \delta^2 \times t_{1/2}^{-1} \quad (1)$$

where δ is the specimen thickness, $t_{1/2}$ the half-rise time required for the rear face temperature rise to reach one-half of its maximum value.

The specific heat capacity of the test specimens was determined by differential scanning calorimetry (DSC 214 Polyma) and a standard specimen with known specific heat capacity. The specific heat capacity can be calculated by the following equation:

$$C_{px} = C_{pS} \cdot \frac{M_S \cdot \Delta T_S}{M_x \cdot \Delta T_x} \quad (2)$$

where M is the mass of the specimen, and ΔT the temperature difference between baseline and maximum temperature values. Subscripts x and S represent the specimen to be tested and the standard specimen, respectively.

Finally, the thermal conductivity λ is calculated from the product of thermal diffusivity α, density d, and specific heat capacity C_p:

$$\lambda = \alpha \cdot d \cdot C_p \quad (3)$$

2.4. Microstructure observation

The as-received Alloy 690 heat transfer tube was sampled by wire electrical discharge machining to observe the microstructure of the alloy. The specimen was mechanically polished with #400, #1000, #2000, and #3000 particle size SiC abrasive paper, and then electropolished with 7% (volume fraction) $HClO_4$ and 93% (volume fraction) ethanol for 1 min at room temperature. The current density was 450 mA/cm^2. It was chemically etched in a diluted bromine solution. Twins and intragranular carbides were observed using SEM (Thermo Scientific Apreo S–USA) at 25 kV.

The quasi-in-situ EBSD of Alloy 690 specimen before and after the EMCT was performed using a JSM7200F field emission SEM fitted with an EDAX EBSD Velocity detector as follows: (1) Select a scanning micro area of the specimen (the section of the tube), namely TN-ND planes, as shown in Fig. 5 under SEM, the collection step size of 1.1 μm is set and perform EBSD scanning on the scanning area of 300 × 1500 μm^2, make fiducial marks on the surface of the specimen and record the data; (2) The specimen is subjected to electromagnetic coupling treatment. (3) Reposition the EBSD scanning area according to the fiducial mark made in (1), perform EBSD scanning at the same collection step size and record the data. (4) The EBSD results of the same micro-region of the specimen before and after the EMCT are compared and analyzed using HKL CHANNEL5 software.

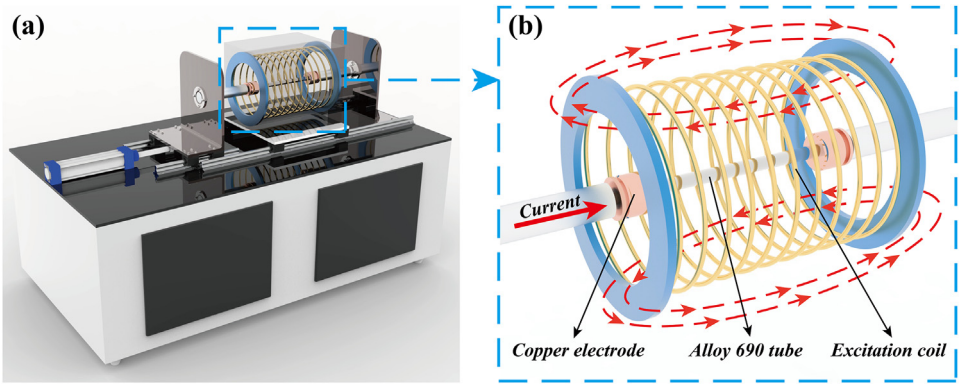

Fig. 1 – Illustration of the experimental process: (a) electromagnetic coupling treatment experiment platform, and (b) schematic of the electromagnetic field distribution during the treatment process.

To observe the effect of EMCT on the dislocations and precipitated phases, a transmission electron microscope (TEM; FEI Talos F200X G2) working at 200 kV was used for TEM diffraction contrast imaging, high-resolution transmission electron microscope (HRTEM) and selective electron diffraction (SAED). After the specimen was cut, mechanically polished, polished, and flushed, the thin foil was prepared by an ion beam thinning apparatus (Gatan 695). The specimen preparation parameters are: ion beam energy 5 Kev, ion gun angle ±8° thinning to the hole; 4 Kev ±4° thinning for 5min; 3 Kev ±3° thinning for 5min. The element contents of the test specimen matrix and precipitated phases were analyzed using the attached energy dispersive spectroscopy (EDS), and microscopic regions of the precipitated phases and their adjacent regions were line-scanned.

3. Results

3.1. *Thermal performance measured*

Fig. 2d shows the thermal conductivity and heat capacity of Alloy 690 after different EMCT experimental parameters, each parameter was measured three times and averaged to reduce random error. The thermal conductivity and the heat capacity of the as-received test specimen are 16.243 W/(m·K) and 0.572 J/(g·K), respectively. Reference lines for the thermal conductivity and heat capacity of the as-received test specimen are drawn with black and red dashed lines in Fig. 2a and b, respectively. The heat capacity of the test specimens hardly changed after the EMCT, and the maximum change rate was controlled within 5%. The thermal conductivity of the specimens after the EMCT has been improved by a varying extent. Keeping the electric field strength constant at 1.5 V, the thermal conductivity of the test specimens showed a trend of increasing and then decreasing with the increase of the magnetic field strength (Fig. 2a). Keeping the magnetic field strength constant at 1.5 T, the thermal conductivity of the test specimens shows the same trend as above with the increase of the electric field strength (Fig. 2b). Among the set parameter gradient groups, the optimal EMCT experimental parameters for electric field strength and magnetic field strength were 1.5 V and 1.5 T, respectively, at which the thermal conductivity grew to 19.089 W/(m·K) with an increase of 17.5%. Fig. 2c compares the effects of as-received (Untreated), electric-only treatment (1.5 V), magnetic-only treatment (1.5 T) and EMCT (1.5 V, 1.5 T) on the thermal conductivity and heat capacity. Both the electric-only treatment and the magnetic-only treatment can improve the thermal conductivity by 5.2% and 9.3%, respectively, while the EMCT has the best effect (17.5%).

3.2. *Microstructures and texture evolutions during the EMCT*

3.2.1. *SEM morphology*

Fig. 3 shows that the as-received Alloy 690 is characterized by equiaxed grains with an average grain size of approximately 170 μm in diameter. Fine continuous precipitates can be observed at the GBs, which are Cr-rich $M_{23}C_6$ carbides confirmed by EDS analysis, as shown in Fig. 3d. The $M_{23}C_6$ phase has a face-centered cubic (FCC) lattice structure and maintains a cubic coherent orientation relationship with the FCC austenite matrix on the precipitation side. The flocculent precipitated phase deposition area consists of fine $M_{23}C_6$ carbides scattered at the junction of three crystals (Fig. 3b). In addition, a small amount of granular $M_{23}C_6$ carbides were found inside the grains (Fig. 3c).

Fig. 4 compares the morphological evolution of precipitates in SEM images before and after the EMCT. The evolution of precipitates can be divided into three parts: at the general GBs,

Table 3 – Processing parameters of EMCT experiments.

Treatment	Specimens number										
	1	2	3	4	5	6	7	8	9	10	11
Electric field intensity (V)	0	1.5	1.5	1.5	1.5	1.5	0	0.5	1	2	2.5
Magnetic field intensity (T)	0	0	0.5	1	1.5	2	1.5	1.5	1.5	1.5	1.5

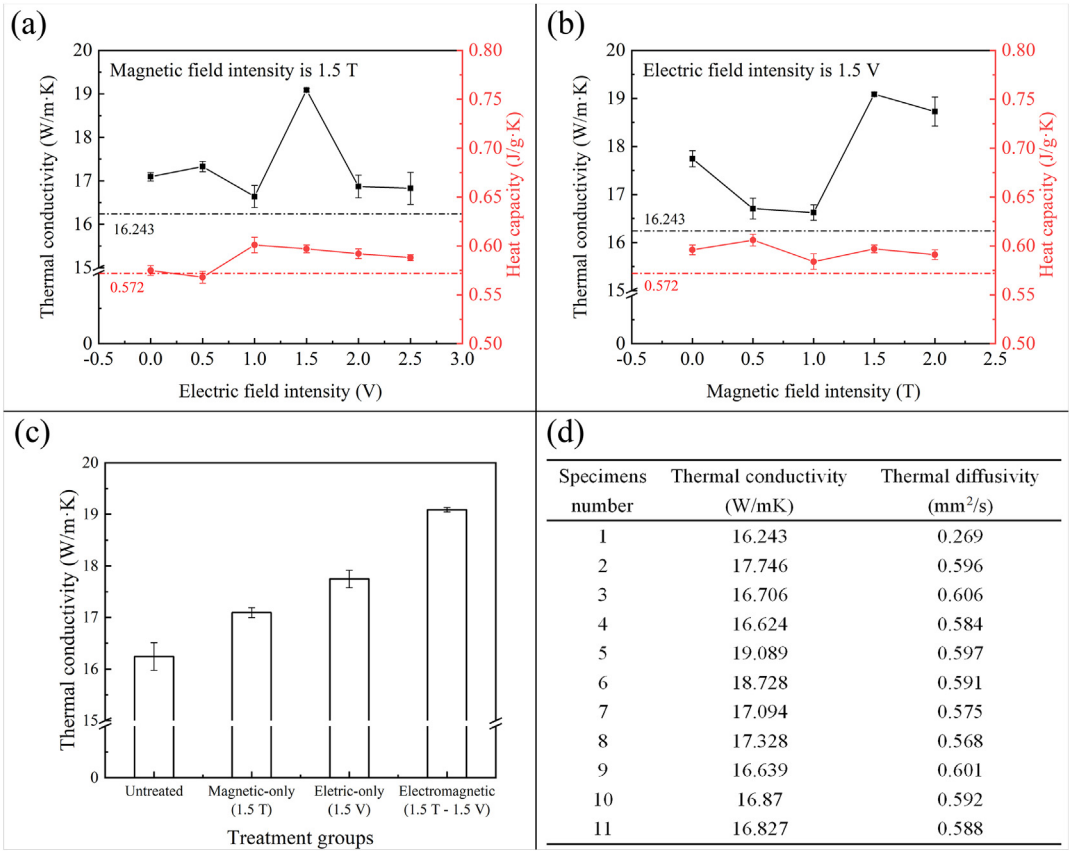

Fig. 2 – Effect of EMCT on thermal conductivity and heat capacity: (a) effect of magnetic field parameters on thermal conductivity and heat capacity, (b) effect of electric field parameters on thermal conductivity and heat capacity, (c) comparison of untreated, electric-only, magnetic-only and EMCT effects, and (d) thermal properties measured.

in the flocculated precipitates accumulation area, and at the twin boundaries. After the EMCT, the amount of $M_{23}C_6$ carbides in the alloy increased, and the newly formed fine $M_{23}C_6$ carbides grew at the interface of the triple crystals. In addition, the originally tiny $M_{23}C_6$ carbides inside the grains (100 nm) grew into acicular precipitates (with an average length of 1–2 μm), especially near the GBs. In the flocculent precipitates accumulation area, the amount of $M_{23}C_6$ carbides in the EMCT specimen is significantly higher than that in the UT specimen. The contrast of precipitates at the twin boundaries is even more obvious. The EMCT specimen has more $M_{23}C_6$ carbides than the UT specimen, both at the transgranular twin boundaries and at the suspended twin boundaries, especially at the non-coherent interface of suspended twin boundaries as shown in Fig. 4.

3.2.2. *EBSD morphology*

Fig. 5 shows the quasi-in-situ EBSD data of Alloy 690 before and after the EMCT. Fig. 5c shows the cross-section of the Alloy 690 heat transfer tube, RD and AD represent the radial and axial directions of the heat transfer tube, respectively, and RD1 and RD2 are two mutually perpendicular radial directions. The band contrast (BC) represents a darker contrast indicating more dislocations (Fig. 5a). From the inverse pole figure (IPF), it can be found that the as-received Alloy 690 has a large number of twins generated during annealing, and the twins consist of transgranular twins and suspended twins (Fig. 5b) [15]. The twinning plane of the FCC crystal is {111} and the twins have a misorientation relationship of <111>//60° with the parent grains. Fig. 5c shows the (001), (101), and (111) pole figures (PFs) of the Alloy 690 specimens. Comparing the IPF and PF before and after the EMCT, it can be seen that the EMCT hardly changed the texture of Alloy 690. A random distribution of (001) and (101) poles is visible in the specimens. The highest texture intensities before and after the EMCT were 4.15 and 4.06 (multiple of random distribution, mrd), respectively, with <111> of grains parallel to AD rolling direction under the specimen coordinate system. This texture is formed by cold rolling deformation of Alloy 690, which is mainly composed of typical Brass, Cu, and S textures. The texture intensity of Alloy 690 decreased slightly after the EMCT, which is due to the $M_{23}C_6$ carbides precipitation behavior in the grains during the EMCT, and the deformed grains before the EMCT rotate in a specific direction with a small amplitude during this process. Consequently, this indicates that Alloy 690 generates low angle grain boundaries (LAGBs) during EMCT, but does not exhibit significant GB shrinkage.

Fig. 6 compares the GB maps before and after the EMCT. The GBs of adjacent grains with a misorientation angle less than 15° are called low angle grain boundaries (LAGBs), where the GBs with a misorientation angle from 2° to 5° are shown in

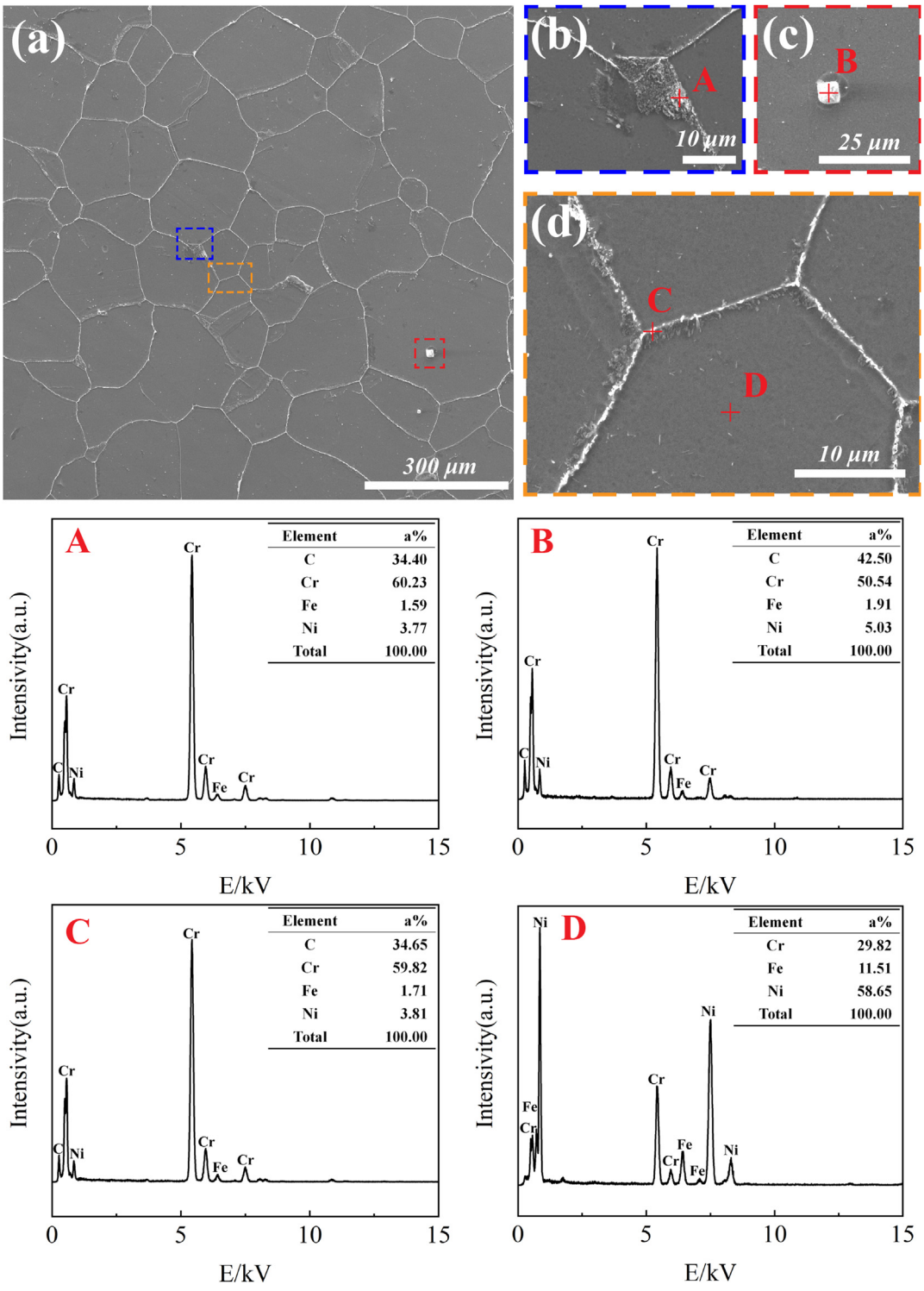

Fig. 3 – SEM images of as-received Alloy 690: (a) macroscopic SEM image, (b) flocculent $M_{23}C_6$ carbides at the triple crystal junction, (c) $M_{23}C_6$ carbides in the grains, and (d) fine continuous $M_{23}C_6$ carbides precipitated at the GBs.

red and those greater than 5°–15° are shown in green. The GBs with a misorientation angle greater than 15° are called high angle grain boundaries (HAGBs) and are shown in black. The amount of all LAGBs increased after the EMCT, especially the LAGBs with misorientation less than 5° increased significantly. This indicates that the newly generated grain boundaries first appeared in the form of subgrain boundaries or LAGBs after the EMCT, which is corroborated with the texture results.

Fig. 7 shows the kernel average misorientation (KAM) of Alloy 690 before and after the EMCT. The minimum and maximum KAM value is represented by blue and red colors,

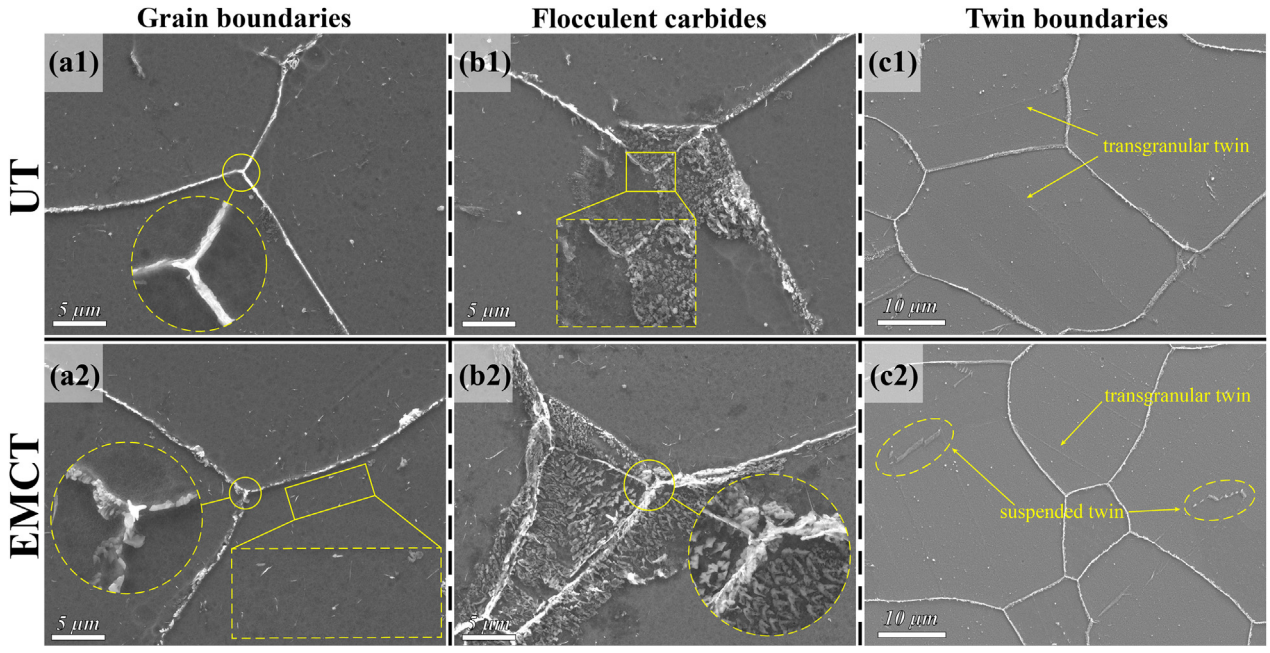

Fig. 4 – Morphological evolution of $M_{23}C_6$ carbides at grain boundaries, flocculent carbides, and twin boundaries, respectively. (a1-c1) UT and (a2-c2) EMCT.

respectively. The KAM distribution can reflect the homogenization degree of plastic deformation and qualitatively analyze the change of orientation gradient inside the grain. The region with a high value indicates a high degree of plastic deformation or high defect density, which is often used to reveal local dislocations and strain energy. After the EMCT, the KAM distribution inside the grains and near the twin boundaries changed significantly. The overall distribution of KAM tended to be uniform, which represents the homogenization of dislocation density. Noted that the KAM value of most twins increased, and the KAM distribution tended to be consistent with the parent grains, as shown in the selected grain regions in Fig. 7.

3.2.3. *TEM morphology*

Fig. 8 shows the TEM bright-field images and corresponding selected area electron diffraction (SAED) pattern. Fig. 8a-d3 show the microstructure of the as-received Alloy 690 and the corresponding SEAD pattern. There are a large amount of dislocation lines inside the grains, forming a complex dislocation net, and some dislocation lines are entangled with each other (Fig. 8a and b). In addition, the dislocation distribution is inhomogeneous, high dislocation density appears in some local areas, and the dislocation-free areas and the dislocation-entangled areas coexist. In contrast, the matrix after the EMCT is cleaner with significantly fewer dislocations, and no dislocation entanglement (Fig. 8e). Fig. 8b and f compare the effect of the EMCT on the microstructure near the twins. It can be found that the as-received specimen is cleaner near the twin boundaries. After the EMCT, a large numbers of dislocations are accumulated at the twin boundaries, and the crossed dislocation lines form a dislocation wall.

High-resolution transmission electron microscope (HRTEM) was used to characterize the interface position between the $M_{23}C_6$ carbide and the precipitation side of the matrix at the GB of Alloy 690 specimens with and without the EMCT. The interplanar spacings of the $M_{23}C_6$ phase and the γ matrix phase were measured to be about 6.19 Å and 2.06 Å, respectively, by observing the HRTEM images. The interplanar spacing of the $M_{23}C_6$ phase is approximately three times that of the matrix phase. There is a cube-to-cube orientation relationship between the $M_{23}C_6$ carbide and the precipitation side of the matrix. The phase interface denoted by the dashed lines in Fig. 8 d2 was a flat interface. The lattice stripes of the matrix at the interface with the $M_{23}C_6$ phase are blurred and have obvious dark areas. This indicates that there are dislocations in this area, resulting in lattice distortion. While the lattice stripes at a similar position after the EMCT are relatively clear, (Fig. 8 h2), indicating that the lattice distortion in this area is not significant.

It can be observed that there are division lines in some $M_{23}C_6$ carbides at the GB of the EMCT specimen, and no fine $M_{23}C_6$ carbide is observed (Fig. 8g). This shows that during the EMCT, the $M_{23}C_6$ carbides grow through the combination of adjacent carbides, and the fine carbides at the GBs gradually dissolve. Consequently, the average size of carbides and the average distance between adjacent carbides will increase.

EDS line scan is performed on the $M_{23}C_6$ carbide and adjacent sides of the matrix. Taking the center of the $M_{23}C_6$ carbide as the starting point, the length of 100 nm to both sides of the matrix is scanned (Fig. 9 a1 and b1). The line scan results of the UT specimen and the EMCT specimen are shown in Fig. 9 a2 and **b2**, respectively. The main elements inside the $M_{23}C_6$ carbide (from −50 to 50 nm) are composed of carbon and chromium. The proportions of these two elements in the UT specimen were about 60% (C) and 40% (Cr), respectively. After the EMCT, the proportion of chromium reached about 60%. In the matrix outside the $M_{23}C_6$ carbide (from −100 to −50 nm,

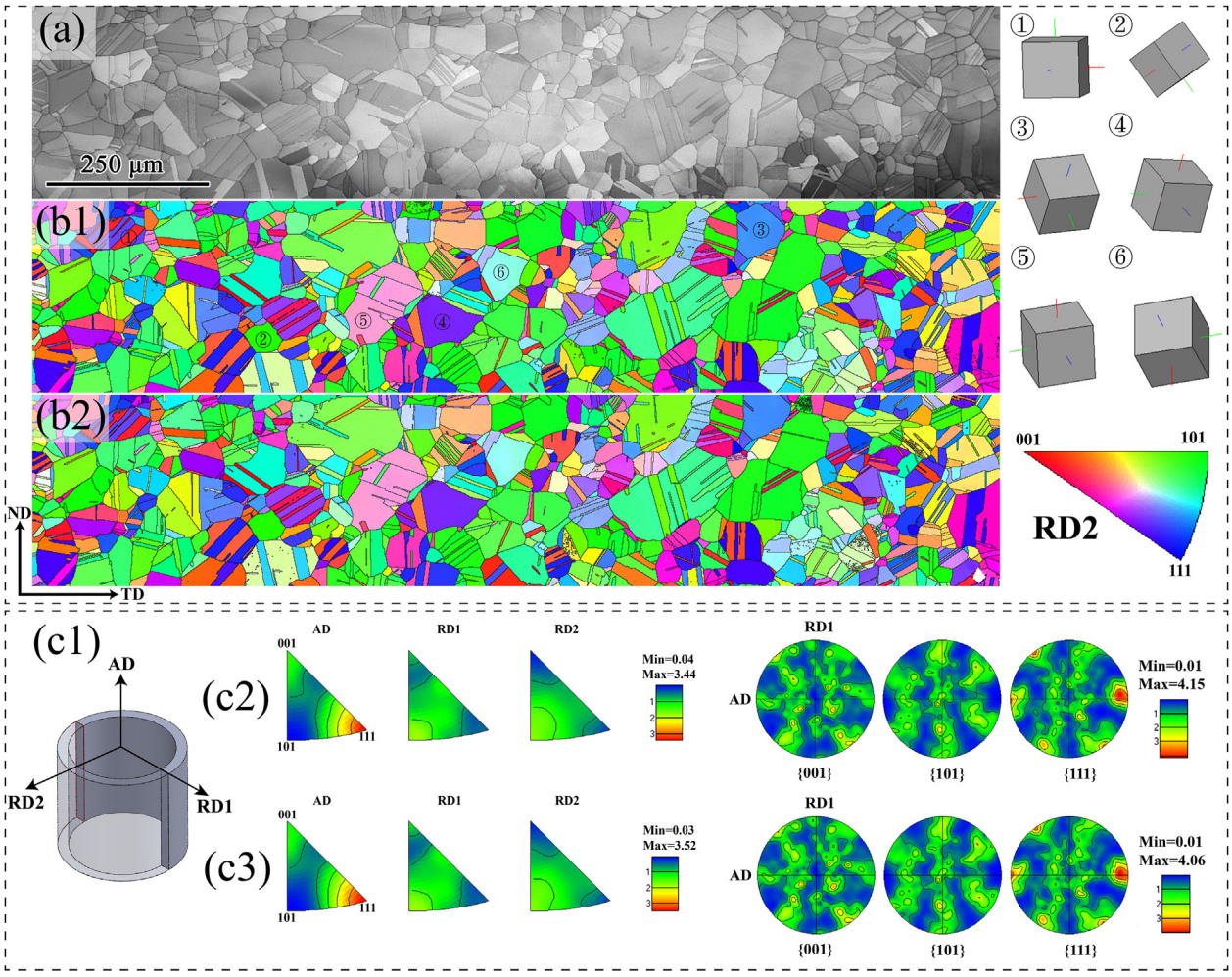

Fig. 5 – EBSD images of the as-received Alloy 690: (a) BC map, (b1) IPF map of UT, (b2) IPF map of EMCT, three-dimensional crystallographic relationship corresponding to different colors of IPF display on the right of figure, (c1) sample coordinate system, (c2) PF map of UT, and (c3) PF map of EMCT.

and from 50 to 100 nm), the elemental composition is mainly nickel, carbon, iron, and chromium. After the EMCT, the proportion of carbon in the matrix decreased by about 20%, and the proportion of solvent nickel atoms in the matrix increased by about 20%. According to the EDS line scan results and TEM images, it can be inferred that the EMCT promotes the precipitation of $M_{23}C_6$ carbides in the Alloy 690, thereby reducing the amount of impurity solute atoms and the lattice distortion in the matrix.

4. Discussion

4.1. *Changes of the thermal conductivity due to the electromagnetic treatment and underlying mechanism*

Heat transfer in alloys is achieved by energy transfer. The carriers of the heat conduction process are free electrons, lattice vibration harmonics (phonons), and electromagnetic radiation (photons). The heat conduction of electromagnetic radiation in the alloy is negligible. The Cr content in Alloy 690 is relatively high, about 30%, the scattering effect of solute atoms in the matrix on electrons is amplified, and the mean free path of electrons is greatly reduced, which is approximately equal to that of phonons. Therefore, the thermal conductivity of the alloy is mainly contributed by electrons and phonons:

$$\lambda = \frac{1}{3} C_V \bar{v} l \tag{4}$$

where C_V is the electrons (phonons) heat capacity per unit volume, the average velocity of electrons (phonons), l the mean free path of electrons (phonons). In the alloy, the factors that disrupt the crystal cycle integrity and distort the alloy matrix, such as point defects, dislocations, and microcracks, will lead to lattice distortion that leads to the scattering of phonons and electrons. This reduces the mean free path of phonons and electrons, thereby, reducing the thermal conductivity of the material [4]. After the EMCT, the number of the $M_{23}C_6$ carbides (Fig. 3) and the proportion of the LAGBs (Fig. 4) have increased, which led to the increase of the scattering of electrons and phonons, resulting in a decrease in thermal

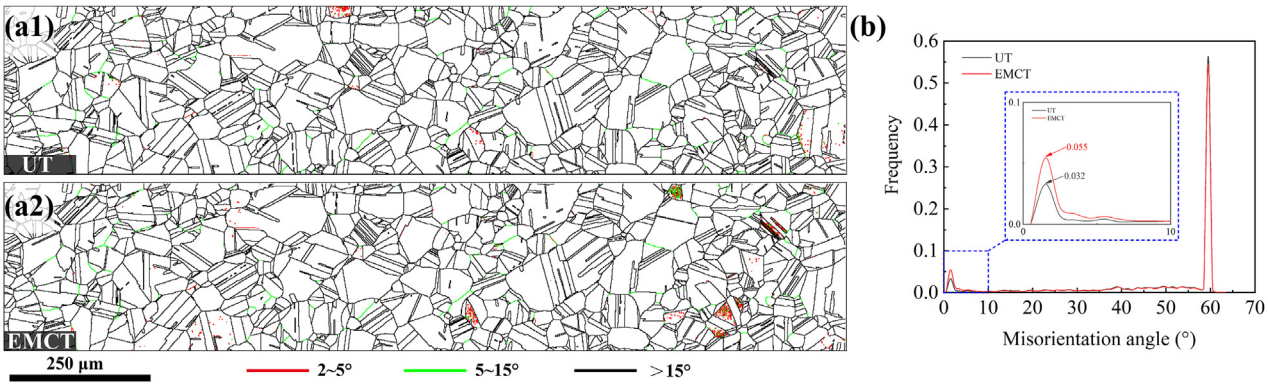

Fig. 6 – EBSD images: (a1) GB maps of UT, and (a2) GB maps of EMCT, in which red, green, and black indicate GBs with misorientation angles of adjacent grains ranging from 2° to 5°, 5° to 15°, and greater than 15°, respectively; (b) misorientation angle distribution, the blue dashed box is an enlarged detail from 0° to 10°.

conductivity. The uniform distribution and annihilation of dislocations (Figs. 7 and 8) and the reduction of solute atoms (Fig. 9) led to an increase in thermal conductivity. Since the number of solute atoms in the alloy is much larger than that of dislocations and other crystal defects, even though the lattice distortion produced by each solute atom is weaker than that of dislocations and other crystal distortions, the overall degree of distortion is higher. Taking all factors into consideration, the thermal conductivity finally increased, indicating that the weakening of lattice distortion caused by precipitation of the solute atoms during the EMCT is a main factor influencing the increase of thermal conductivity. According to the microstructure results, this study suggests that the main factors influence the thermal conductivity of the alloy in the following order: solute atoms > dislocations > precipitates > grain boundaries/twin boundaries.

From the measured results presented in Fig. 2, it can be found that both the electric-only treatment and the magnetic-only treatment may be able to improve the thermal conductivity to some extent, but the EMCT has the best effect. The EMCT cannot be simply viewed as a superposition of the electric and magnetic field treatments. Thermal conductivity result does not present a linear relationship with electric field intensity and magnetic field intensity. It showed a trend of firstly increasing and then decreasing with the increase of the magnetic field intensity and electric field intensity. Excessive electromagnetic field parameters could weaken the strengthening effect, and the main reason for this phenomenon is due to the dislocation pile-ups caused by excessive dislocation motion. In this study, the process design of the EMCT mainly considered the dislocation density and the solid solubility of the material.

4.2. *Effect of the electromagnetic treatment on the dislocations*

The change of KAM distribution represents the change of dislocation distribution. The total volume dislocation density shows a trend of homogenization. The dislocation density near the GBs changes significantly. It is speculated that there

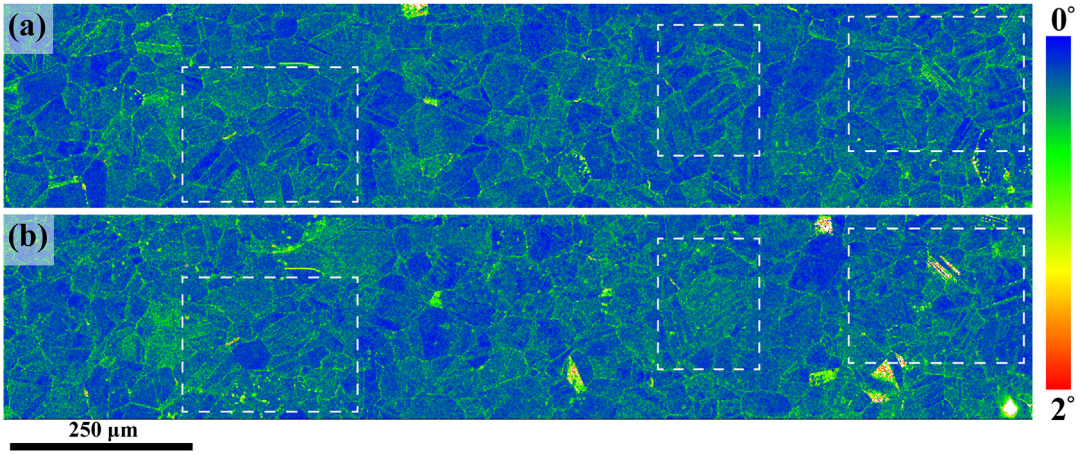

Fig. 7 – KAM maps of the (a) UT and (b) EMCT, the KAM value of the twins in the white dashed box area increases significantly and the KAM distribution tends to be consistent with the parent grains.

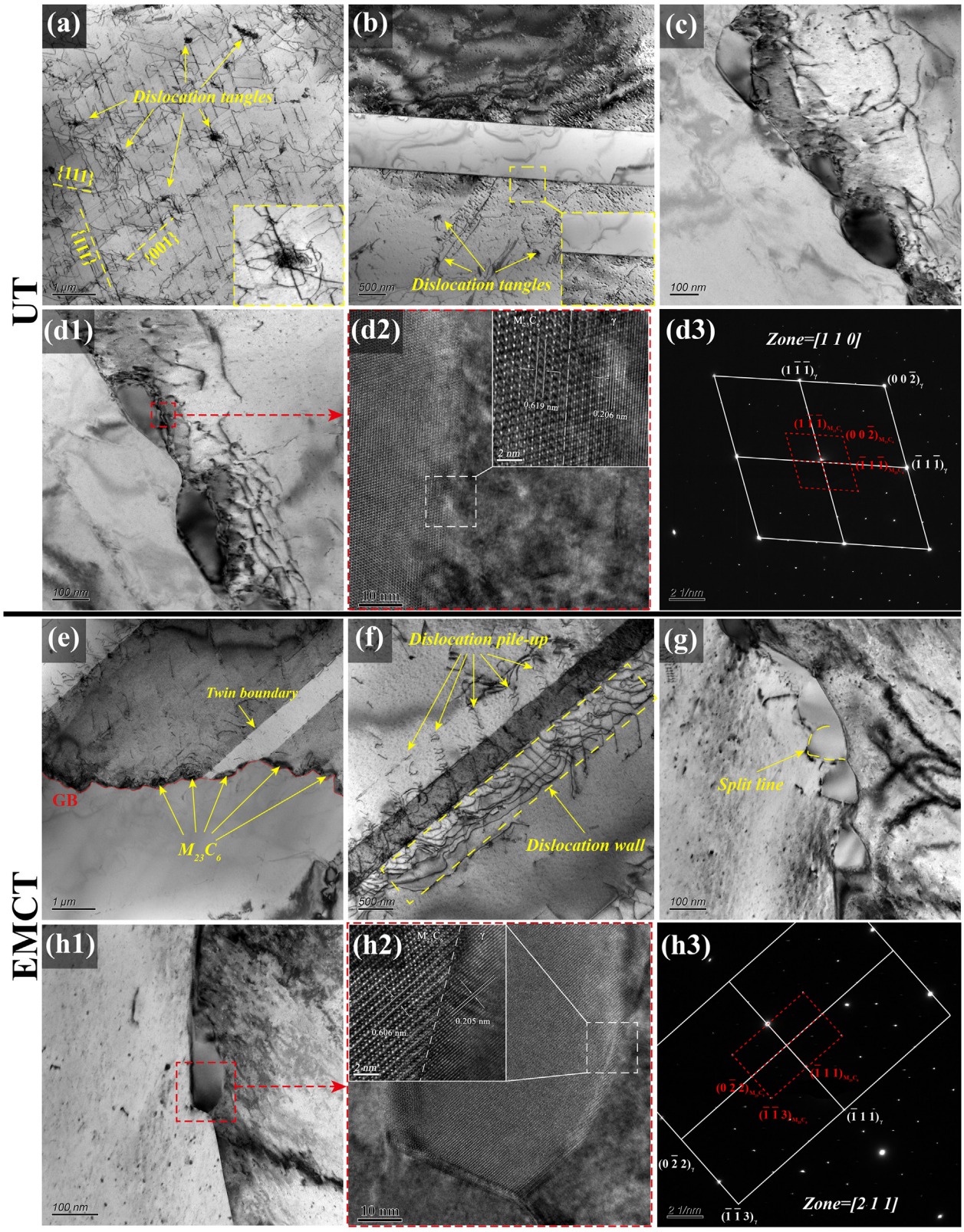

Fig. 8 – TEM images and corresponding SAED patterns of precipitated phase characteristics: (a-d3) UT and (e-h3) EMCT.

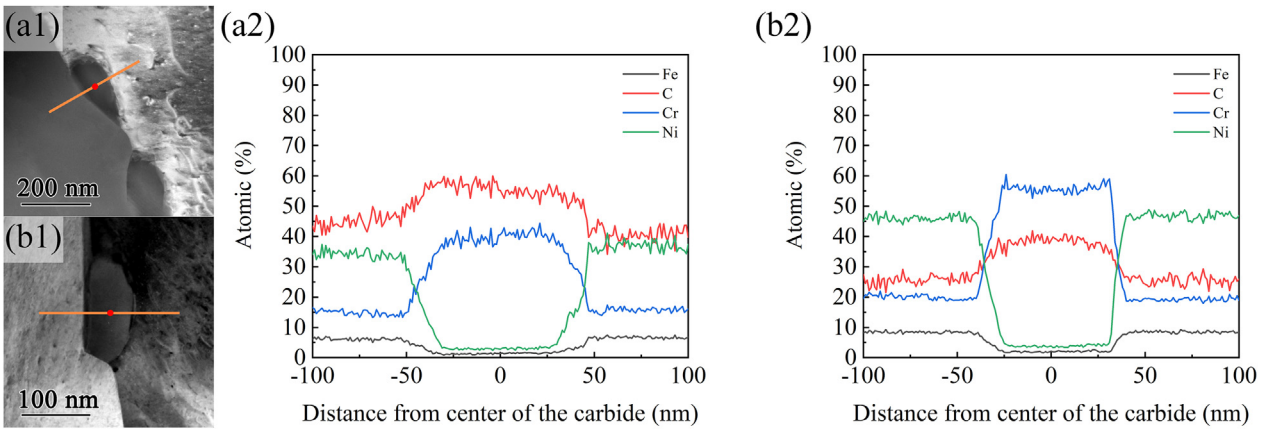

Fig. 9 – EDS line scan on the $M_{23}C_6$ carbide and adjacent sides of the matrix: (a) UT and (b) EMCT.

may be slipping and climbing of dislocations in the GBs region. This speculation is consistent with the change of GB angle in Fig. 6. Beckett et al. [16] believe that $M_{23}C_6$ carbide is formed by dislocation migration, this also confirms that the EMCT will promote the precipitation of $M_{23}C_6$ in Alloy 690.

The above results indicate that the thermal conductivity of the specimens was enhanced by the EMCT, i.e., the specimens underwent lattice rearrangement during the EMCT process. Magnetoplasticity and electroplasticity are closely related to the generation and motion of dislocations. The structure and distribution of dislocations in the specimens can reflect the mechanism of the electroplasticity and magnetoplasticity effects on the dislocations during the EMCT process.

Dislocation is a kind of crystal defect, and its existence will have a corresponding impact on the properties of the alloy. The higher the dislocation density, the more serious the lattice distortion caused by dislocations in the alloy, and the lower the thermal conductivity of the alloy. The presence of dislocations increases the energy of the crystal containing dislocations, and this part of the energy is called dislocation energy. Dislocation energy consists of two parts, namely elastic strain energy and core energy. The core energy of dislocation is very small and can generally be ignored. The elastic strain energy is the energy stored by dislocations that distort the surrounding lattice to some extent. The elastic strain energy per unit length of dislocation is given by the integral [17]:

$$E_{el}^{screw} = \frac{Gb^2}{4\pi}\int_{r_0}^{R}\frac{dx}{x} = \frac{Gb^2}{4\pi}\ln\left(\frac{R}{r_0}\right) \tag{5}$$

$$E_{el}^{edge} = \frac{Gb^2}{4\pi(1-\upsilon)}\int_{r_0}^{R}\frac{dx}{x} = \frac{Gb^2}{4\pi(1-\upsilon)}\ln\left(\frac{R}{r_0}\right) \tag{6}$$

where G is the second parameter of Lamé constant, which can be thought of as the shear modulus, b the magnitude of Burgers vector, ν the Poisson ratio, R the shield length, r_0 the radius of the dislocation core.

Dislocations are generally curved and irregular, but the Burgers vector is the same all along its length, therefore, the curved dislocation can be regarded as a mixed dislocation combining edge dislocation and screw dislocation. Let the angle between the Burger vector b and the dislocation line be θ. The elastic field of a mixed dislocation is the superposition of the fields of its edge and screw parts. As there is no interaction between them, the total elastic energy is simply the sum of the edge and screw energies with b replaced by $b\sin\theta$ and $b\cos\theta$, respectively:

$$\begin{aligned} E_{el}^{mixed} &= \left[\frac{Gb^2\sin^2\theta}{4\pi(1-\upsilon)} + \frac{Gb^2\cos^2\theta}{4\pi(1-\upsilon)}\right]\ln\left(\frac{R}{r_0}\right) \\ &= \frac{Gb^2}{4\pi(1-\upsilon)}(1-\upsilon\cos^2\theta)\ln\left(\frac{R}{r_0}\right) \end{aligned} \tag{7}$$

A large numbers of paramagnetic substances are present in the Alloy 690, such as dislocations and precipitates. Dislocations exhibit paramagnetism due to the abundance of free electrons. The $M_{23}C_6$ phase is mainly composed of Cr and Fe elements and is a typical paramagnetic phase. When there is a magnetic field, the dislocations inside the material are magnetized by the magnetic field, resulting in magnetic stress. The strain energy E_{mag} obtained by the dislocation in the magnetic field can be expressed as [18]:

$$E_{mag} = \frac{b^2H_0h_0r_0}{8(1-\upsilon)}(\mu-1)(1-2\nu)(2\mu-1)\ln\frac{R}{r_0} \tag{8}$$

where H_0 represents the magnetic intensity of the external magnetic field, h_0 is the magnetic intensity due to the magnetic magnetization of dislocations, and μ the displacement vector.

In the presence of both elastic stress field and magnetic field, the total dislocation energy E_{total} can be expressed as:

$$\begin{aligned} E_{total} &= E_{el}^{mixed} + E_{mag} \\ &= \frac{Gb}{4(1-\upsilon)}\left[\frac{Gb}{\pi}(1-\upsilon\cos^2\theta) + \frac{H_0h_0r_0}{2}(\mu-1)(1-2\nu)(2\mu-1)\right]\ln\left(\frac{R}{r_0}\right) \end{aligned} \tag{9}$$

For $\mu > 1$, E_{mag} is positive, the total strain energy of dislocations increases, which enhances the de-pinning effect of

dislocations from the pinning center, thereby increasing the potential for dislocation movement.

During the rolling of the Alloy 690 heat transfer tube, the movement of dislocations at obstacles (such as precipitations or grain boundaries) is hindered, and dislocations are entangled and accumulated (Fig. 8a and b). These high-density dislocation regions become new obstacles for dislocation slip. During the EMCT process, the magnetic field meets the electron excitation conditions. The energy state of the bonding electrons of atoms in the dislocation pinning region changes from the ground state (singlet state) to an excited state (triplet state) with lower binding energy. Compared to the singlet state, the triplet state exhibits the characteristics of lower energy storage and increased stability, which corresponds to a lower barrier for dislocation movement. The binding ability between electron pairs is weak, and thus the interaction force between dislocations and obstacles weakens or disappears, and the binding bonds are easily broken. The migration of vacancies or impurity atoms is promoted leading to the de-pinning of dislocations [19–23].

After the de-pinning of dislocations by the magnetoplastic effect, the drift electrons exert a force on the dislocation owing to the momentum transfer as the electrons collide with atoms, i.e., the electron wind force [24,25]. The electron wind force per unit dislocation length [26]:

$$F_{ew} = \rho_d e n_e J (N_d)^{-1} \tag{10}$$

where ρ_d is the resistivity per unit dislocation length, N_d the dislocation density, n_e the electron density, e the electron charge, and J the current density.

Alloy 690 is a FCC lattice structure alloy with low stacking fault energy. The ability of dislocation climb and cross-slip is weak, and dislocations are easy to accumulate, forming a uniformly distributed complex network. Driven by the electron wind, the dislocation lines slip along the current direction and are blocked at the GBs or twin boundaries. The dislocations are arranged parallel to each other and are not uniformly distributed. The closer the dislocations are to the twin boundary, the closer they are to each other. The phenomenon of massive screw dislocation cross-slip occurs due to the formation of a sustained dislocation pile-up group [20]. The dislocations pile-up group forms a dislocation wall around the twin boundaries (Fig. 8f). The twin boundaries interact with dislocations, and the dislocations around the twin boundaries become entangled resulting in the bending of dislocation lines. The dislocations entangled with each other are easily fixed by the precipitates on the grain boundaries, thus the dislocations are pinned again. This also explains why the thermal conductivity decreases in Fig. 2b when the electric field parameter is too large.

The side effects brought by the current have to be considered here, namely the skin effect and the Joule heating effect [27]. When a pulse current or an alternating electromagnetic field is applied, the current distribution in the specimen is not uniform. The current is concentrated in the thin layer on the outer surface of the conductor, and the closer it is to the surface of the conductor, the greater the current density, i.e. skin effect. The skin effect of the induced current caused by the magnetic field is negligible in this study. The skin depth $\Delta\delta$ was calculated using the equation [26]:

$$\Delta\delta = \left(\frac{\pi f \mu}{\rho}\right)^{-1/2} \tag{11}$$

where f is the frequency of the pulse current, μ and ρ the permeability and resistivity of the specimen, respectively. In this study, $f = 50Hz$, $\mu = 1.00027 \times 10^{-4} H/m$, and $\rho = 116 \times 10^{-8} \Omega \cdot m$. Substituting the above values into Eq. (11), the estimated value of $\Delta\delta$ is calculated to be 8.6 mm, which is much larger than the thickness of the specimen (1.02 mm) in this study. It can be concluded that the current in this EMCT experiment is uniformly distributed throughout the specimen cross-section.

The temperature increment by the Joule heating effect can be evaluated based on the following equation [28]:

$$\Delta T = \int_0^t \rho J^2(t) (C_p d)^{-1} dt \tag{12}$$

where $J(t)$ is the current density at time t, $\rho = 116 \times 10^{-8} \Omega \cdot m$ the resistivity, $d = 8.13 \times 10^3 kg/m^3$ the density, $C_p = 579 J/(kg \cdot K)$ the specific heat. In this study, $J(t)$ is assumed to be the maximum current density $J_{max} = 3 \times 10^6 A/m^2$, the current application time is 250 s, and the room temperature is 25 °C, thus the calculated temperature is about 579 °C, which is well below the annealing temperature of 1050 °C. This indicates that the side effect of the Joule heating effect was not the decisive factor for plastic deformation [24,29], which explains why the texture of Alloy 690 in Fig. 5 does not change significantly.

4.3. *Effect of the electromagnetic treatment on solute atoms and precipitation behavior of $M_{23}C_6$ phase*

Due to electroplasticity, the electric current enhances the atomic diffusion [30–32]. The current through the specimen can provide an additional driving force for the chemical potential of atomic diffusion, the effect of electric current on the steady-state atomic drift flux of atoms in metals is given by Nernst–Einstein equation:

$$\Phi = \frac{N_i D}{kT}\left(Z^* e \rho J - \Omega \frac{\partial \sigma}{\partial x} + kT \frac{\partial \ln X_i}{\partial x}\right) \tag{13}$$

where N_i is the concentration of the ith solute, D the pertinent diffusion coefficient, k the Boltzmann constant, T the absolute temperature, Z^* the effective valence, which for many metals is of the order of 10, e the electron charge, ρ the resistivity, J the current density, $-\frac{\partial \sigma}{\partial x}$ the stress gradient, Ω the atom volume, X_i the concentration of the ith solute. The second term is that the electrons flow to the negative electrode and the atoms drift to the positive electrode, forming the back stress generated by the opposing chemical potential. The third term is the chemical

potential gradient of the composition in the alloy. According to Eqs. 10 and 13, when the current density J increases, the drift flux of atoms accelerates, and the electron wind formed by the collision of high-speed electrons with atomic nuclei increases, which contributes to dislocation motion and further provides a potential for untangling dislocations.

The enhancement of atomic diffusion leads to the segregation of solute atoms on dislocation lines. The content of solute atoms on the dislocation line increases, which meets the composition conditions required for the formation of the $M_{23}C_6$ phase. Dislocation lines can act as short-circuit channels for diffusion and reduce the activation energy of diffusion, thereby accelerating the nucleation process [31]. The dislocations and the solute atoms form a precipitate phase. This consumes a large number of dislocations and vacancies as nucleation sites during the formation of precipitates, and the energy released by the ordered rearrangement of dislocations also provides the impetus for nucleation. Dislocation nucleation leads to dislocation annihilation and lower dislocation density. When the solute atoms are dissolved in the matrix, lattice distortion occurs owing to the size difference between the solute atoms and the solvent atoms, changing the lattice parameter c/a, and shortening the mean freedom of electrons and phonons by substituting Ni atoms. Since the unit cell of $M_{23}C_6$ carbide is composed of 92 metal atoms (mainly Cr atoms) and 24 C atoms, occupying the unit cell volume of 27 matrices, there are 108 metal atoms in the matrix in the same volume [33–35]. Therefore, the more the $M_{23}C_6$ phase precipitates, the lower the lattice distortion of the solute atoms in the alloy. As can be seen from Fig. 4 that the amount of $M_{23}C_6$ phases precipitated in the EMCT specimen is more than that in the UT specimen, so the lattice distortion caused by the solute atoms is smaller. From the HRTEM image (Fig. 8), it can be seen that the lattice stripes at the interface between $M_{23}C_6$ carbide and matrix become clearer after the EMCT. The EDS line scan results show that after the EMCT, the precipitation of $M_{23}C_6$ carbides in Alloy 690 reduces the amount of heterogeneous solid solution atoms in the matrix. The lattice distortion in the Alloy 690 matrix is reduced and the thermal conductivity is improved.

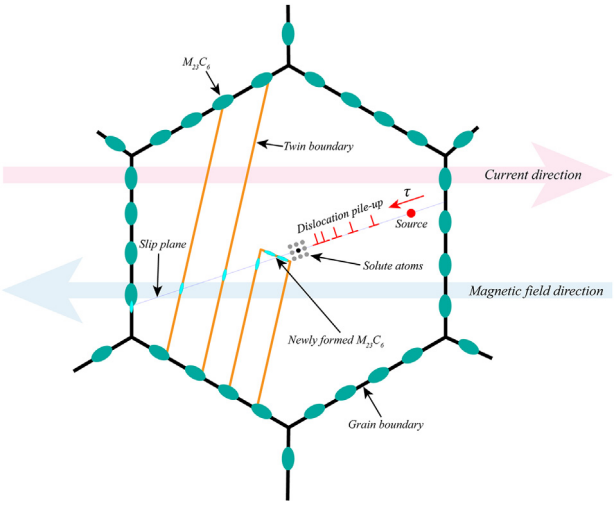

Fig. 10 – Schematic diagram of the effect of the EMCT on the microstructure evolution.

The EMCT induces the precipitation of $M_{23}C_6$ in Alloy 690, which has two effects on the thermal conductivity: Firstly, the newly formed continuously distributed $M_{23}C_6$ phase acts as a scattering center for phonons and electrons, reducing the thermal conductivity of the material. Secondly, with the precipitation of the $M_{23}C_6$ phase, the amount of solute atoms in the matrix decreases, the scattering effect of solute atoms on phonons and electrons decreases, and the mean free paths of phonons and electrons increase, and thus the thermal conductivity of the alloy increases. According to the results of thermal conductivity shown in Fig. 2, the reduction of solute atoms in the matrix has a greater effect on improving thermal conductivity than the increase in precipitates on reducing thermal conductivity.

Fig. 10 presents the schematic diagram of the effect of the EMCT on the microstructure evolution. The mechanism of the EMCT regulating the thermal conductivity of Alloy 690 can be summarized as follows: 1) The magnetic field provides the impetus for the de-pinning of the dislocations, and the magnetic vibrations also provide additional energy for the movement of the dislocations; 2) The electric field exerts the electron wind force on the dislocations, causing the dislocations to move in the direction of electron drift, i.e., the opposite direction of the current, and the dislocation pile-up groups are formed at the obstacles (grain boundaries, twin boundaries or precipitates). Further, the electric field also accelerates the diffusion process of solute atoms; 3) Dislocations and vacancies act as nucleation sites of the precipitation phase and release their energy to provide nucleation driving force, and the $M_{23}C_6$ phase is formed with the segregated solute atoms. The result of the whole EMCT process is that the lattice distortion of the Alloy 690 matrix is reduced, and the scattering effect on electrons and phonons is weakened, to achieve the purpose of improving the thermal conductivity.

5. Conclusions

For the first time, electromagnetic coupling treatment of a nickel-based alloy - Alloy 690, were attempted and studied in great detail with a view to observing the microstructure evolution under the influences of the electromagnetic coupling field, based on which the resulting thermal properties were characterized. The main conclusions can be drawn from this effort as follows:

1) Both the magnetic-only treatment and the electric-only treatment are able to improve the thermal conductivity of the Alloy 690 to some extent. However, the electromagnetic coupling treatment leads to a much better result, with an increase in the thermal conductivity by 17.5%.
2) It is identified that the Joule heating effect and skin effect are not the main factors leading to the evolution of microstructure. The electromagnetic coupling treatment does not significantly alter the texture of the alloy treated.
3) It is demonstrated that the electromagnetic coupling treatment promoted the disentanglement and movement of dislocations, and induced precipitation of the solute atoms, which will reduce the lattice distortion of the

matrix and provide nucleation sites for the precipitation of carbides. The $M_{23}C_6$ phase mainly precipitated at the grain boundary and the twin boundaries, especially at the incoherent interface of suspended twins, and a small amount of acicular $M_{23}C_6$ phase precipitated in the intragranular matrix near the grain boundaries. The reduction of solute atoms in the matrix has a greater effect on improving thermal conductivity than the increase in precipitates on reducing thermal conductivity.

In this paper, a novel material treatment method in the form of electromagnetic coupling treatment is presented. By applying this method thermal conductivity of the nickel-based alloy has been improved significantly. The underlying mechanisms behind this improvement are also examined and discussed in great detail. The developed electromagnetic coupling treatment technology represents a novel enabling technology improving the thermal conductivity of nickel-based superalloys. The results achieved from this study can serve as important technical guidance to the design and research of small-scale nuclear power reactors since the size-range of the corresponding components is suitable for this kind of treatment with a treatment facility on a reasonable scale. At the same time, the presented work in this paper also shows a new approach of studying the thermal properties of other superalloys.

Definition of the Parameters and Variables

Parameter/Variable Definition

Parameter/Variable	Unit	Definition/Remarks
α	mm^2/s	Thermal diffusivity
δ	mm	Specimen thickness
$t_{1/2}$	s	Half-rise time required for the rear face temperature rise to reach one half of its maximum values
C_p	J/(kg·K)	Specific heat capacity
d	kg/m^3	Density
λ	W (m·K)	Thermal conductivity
E_{el}^{screw}	J	Elastic strain energy of screw dislocation
E_{el}^{edge}	J	Elastic strain energy of edge dislocation
E_{el}^{mixed}	J	Elastic strain energy of mixed dislocation
E_{mag}	J	Strain energy obtained by the dislocation in the magnetic field
E_{total}	J	Total strain energy
G	N/m^2	Shear modulus
θ	°	Angle between the Burger vector and the dislocation line
b	m	Burgers vector
F_{ew}	N	Electron wind force
R	m	Shield length
r_0	m	Radius of the dislocation core
υ	/	Poisson's ratio
μ	/	Displacement vector
H_0	A/m	Magnetic intensity of the external magnetic field
h_0	A/m	Magnetic intensity due to the magnetic magnetization of dislocations
F_{ew}	N	Electron wind force per unit dislocation length
ρ_d	Ω·m	Resistivity per unit dislocation length
N_d	$1/m^2$	Dislocation density
n_e	C/m^3	Electron density
e	C	Electron charge
J	A/m^2	Current density
$\Delta\delta$	m	Skin depth
f	Hz	Frequency of the pulse current
μ	H/m	Magnetic permeability
ΔT	°C	Temperature increment by Joule heating effect
Φ	$mol/(m^2 \cdot s)$	Steady-state atomic drift flux
N_i	mol/L	Concentration of the ith solute
D	m^2/s	Pertinent diffusion coefficient
k	J/K	Boltzmann constant
T	°C	The absolute temperature
Z^*	C	Effective valence
σ	MPa	Stress
Ω	m^3	Atom volume
X_i	mol/L	Concentration of the ith solute

Declaration of Competing Interest

The authors declare that they have no known competing financial interests or personal relationships that could have appeared to influence the work reported in this paper.

Acknowledgements

The authors wish to acknowledge the financial support by the National Natural Science Foundation of China, China (No. 51705348) and the Science Foundation of Yibin Government and Sichuan University, China (No. 2020CDYB-10). We appreciate Wang Hui from the Analytical & Testing Center of Sichuan University for her help with BSE characterization and Sinoma Institute of Materials Research (Guang Zhou) Co., Ltd. For the TEM/HRTEM test.

REFERENCES

[1] Rudajevová A, von Buch F, Mordike BL. Thermal diffusivity and thermal conductivity of MgSc alloys. J Alloys Compd 1999;292(1):27–30. https://doi.org/10.1016/S0925-8388(99)00444-2.

[2] Yu Z, Xu C, Meng J, Zhang X, Kamado S. Microstructure evolution and mechanical properties of as-extruded Mg-Gd-Y-Zr alloy with Zn and Nd additions. Mat Sci Eng A-Struct 2018;713:234–43. https://doi.org/10.1016/j.msea.2017.12.070.

[3] Lv B, Peng J, Wang Y, An X, Zhong L, Tang A, et al. Dynamic recrystallization behavior and hot workability of Mg-2.0Zn-0.3Zr-0.9Y alloy by using hot compression test. Mater Des 2014;53:357–65. https://doi.org/10.1016/j.matdes.2013.07.016.

[4] Rudajevová A, Lukč P. Comparison of the thermal properties of AM20 and AS21 magnesium alloys. Mat Sci Eng A-Struct 2005;397(1):16–21. https://doi.org/10.1016/j.msea.2004.12.036.

[5] Pan H, Pan F, Peng J, Gou J, Tang A, Wu L, et al. High-conductivity binary Mg-Zn sheet processed by cold rolling and subsequent aging. J Alloys Compd 2013;578:493–500. https://doi.org/10.1016/j.jallcom.2013.06.082.

[6] Tong X, You G, Ding Y, Xue H, Wang Y, Guo W. Effect of grain size on low-temperature electrical resistivity and thermal conductivity of pure magnesium. Mater Lett 2018;229:261–4. https://doi.org/10.1016/j.matlet.2018.07.037.

[7] Ying T, Zheng MY, Li ZT, Qiao XG. Thermal conductivity of as-cast and as-extruded binary Mg-Al alloys. J Alloys Compd 2014;608:19–24. https://doi.org/10.1016/j.jallcom.2014.04.107.

[8] Ying T, Zheng MY, Li ZT, Qiao XG, Xu SW. Thermal conductivity of as-cast and as-extruded binary Mg-Zn alloys. J Alloys Compd 2015;621:250–5. https://doi.org/10.1016/j.jallcom.2014.09.199.

[9] Rudajevová A, Lukč P. Interfacial effects on the thermal conductivity of QE22 alloy in SiC/QE22 composites. Mat Sci Eng A-Struct 2002;324(1):118–21. https://doi.org/10.1016/S0921-5093(01)01292-8.

[10] Rudajevová A, Stankě M, Lukč P. Determination of thermal diffusivity and thermal conductivity of Mg-Al alloys. Mat Sci Eng A-Struct 2003;341(1):152–7. https://doi.org/10.1016/S0921-5093(02)00233-2.

[11] Rudajevová A, Kiehn J, Kainer KU, Mordike BL, Lukc P. Thermal diffusivity of short-fibre reinforced Mg-Al-Zn-Mn alloy. Scripta Mater 1998;40(1):57–62. https://doi.org/10.1016/S1359-6462(98)00390-X.

[12] Yuan M, Wang J, Wang L, Zhong F, Huang K, Tian Y. Electromagnetic coupling field strengthening of WC-TiC-Co cermet tools. Ceram Int 2021;47(3):3747–59. https://doi.org/10.1016/j.ceramint.2020.09.232.

[13] Zhang Q, Huang K, Wang J, Wang L, Yuan M, Tian Y, et al. Effect of pulse electromagnetic coupling treatment on thermal conductivity of WC-8Co cemented carbide. Ceram Int 2021;47(16):22683–92. https://doi.org/10.1016/j.ceramint.2021.04.283.

[14] Yonezawa T. 2.08 - nickel alloys: properties and characteristics. In: Konings RJM, editor. Comprehensive nuclear materials. 1st. Oxford: Elsevier; 2012. p. 233–66.

[15] Shimada M, Kokawa H, Wang ZJ, Sato YS, Karibe I. Optimization of grain boundary character distribution for intergranular corrosion resistant 304 stainless steel by twin-induced grain boundary engineering. Acta Mater 2002;50(9):2331–41. https://doi.org/10.1016/S1359-6454(02)00064-2.

[16] Beckitt FR, Clark BR. The shape and mechanism of formation of $M_{23}C_6$ carbide in austenite. Acta Metall 1967;15(1):113–29. https://doi.org/10.1016/0001-6160(67)90159-9.

[17] Hirth JP, Loethe J. Theory of dislocations. 1st. New York: Wiley Interscience; 1982.

[18] Zhao-Long L, Tian-You F, Hai-Yun H. Possible mechanism of plasticity influenced by magnetic field. Chin Phys Lett 2006;23(1):175–7. https://doi.org/10.1088/0256-307x/23/1/051.

[19] Bhaumik S, Molodova X, Molodov DA, Gottstein G. Magnetically enhanced recrystallization in an aluminum alloy. Scripta Mater 2006;55(11):995–8. https://doi.org/10.1016/j.scriptamat.2006.08.018.

[20] Ding Q, Zhang Y, Chen X, Fu X, Chen D, Chen S, et al. Tuning element distribution, structure and properties by composition in high-entropy alloys. Nature 2019;574(7777):223–7. https://doi.org/10.1038/s41586-019-1617-1.

[21] Kris RE, Fleurov V, Molotskii MI. Internal friction of dislocations in a magnetic field. Phys Rev B 1995;51(18):12531–6. https://doi.org/10.1103/PhysRevB.51.12531.

[22] Golovin YI. Mechanochemical reactions between structural defects in magnetic fields. J Mater Sci 2004;39(16):5129–34. https://doi.org/10.1023/B:JMSC.0000039196.60100.74.

[23] Alshits VI, Darinskaya EV, Koldaeva MV, Petrzhik EA. Magnetoplastic effect: basic properties and physical mechanisms. Crystallogr Rep 2003;48(5):768–95. https://doi.org/10.1134/1.1612598.

[24] Xiang S, Zhang X. Dislocation structure evolution under electroplastic effect. Mat Sci Eng A-Struct 2019;761:138026. https://doi.org/10.1016/j.msea.2019.138026.

[25] Troitskii O. Electromechanical effect in metals. Pis'Ma Zhurn. Experim. Teoret. Fiz. 1969;10.

[26] Okazaki K, Kagawa M, Conrad H. An evaluation of the contributions of skin, pinch and heating effects to the electroplastic effect in titatnium. Mater Sci Eng 1980;45(2):109–16. https://doi.org/10.1016/0025-5416(80)90216-5.

[27] Kinsey B, Cullen G, Jordan A, Mates S. Investigation of electroplastic effect at high deformation rates for 304SS and Ti-6Al-4V. CIRP Annals 2013;62(1):279–82. https://doi.org/10.1016/j.cirp.2013.03.058.

[28] Sprecher AF, Mannan SL, Conrad H. On the temperature rise associated with the electroplastic effect in titanium. Scripta Metall 1983;17(6):769–72. https://doi.org/10.1016/0036-9748(83)90491-X.

[29] Sprecher AF, Mannan SL, Conrad H. Overview no. 49: on the mechanisms for the electroplastic effect in metals. Acta Metall 1986;34(7):1145–62. https://doi.org/10.1016/0001-6160(86)90001-5.

[30] Kim M, Lee K, Oh KH, Choi I, Yu H, Hong S, et al. Electric current-induced annealing during uniaxial tension of aluminum alloy. Scripta Mater 2014;75:58–61. https://doi.org/10.1016/j.scriptamat.2013.11.019.

[31] Bertolino N, Garay J, Anselmi-Tamburini U, Munir ZA. Electromigration effects in Al-Au multilayers. Scripta Mater 2001;44(5):737–42. https://doi.org/10.1016/S1359-6462(00)00669-2.

[32] Samuel EI, Bhowmik A, Qin R. Accelerated spheroidization induced by high intensity electric pulse in a severely deformed eutectoid steel. J Mater Res 2010;25(6):1020–4. https://doi.org/10.1557/JMR.2010.0140.

[33] Lewis MH, Hattersley B. Precipitation of $M_{23}C_6$ in austenitic steels. Acta Metall 1965;13(11):1159–68. https://doi.org/10.1016/0001-6160(65)90053-2.

[34] Liu Y, Jiang Y, Xing J, Zhou R, Feng J. Mechanical properties and electronic structures of $M_{23}C_6$ (M = Fe, Cr, Mn)-type multicomponent carbides. J Alloys Compd 2015;648:874–80. https://doi.org/10.1016/j.jallcom.2015.07.048.

[35] Adhikari P, San S, Zhou C, Sakidja R, Ching W. Electronic structure and mechanical properties of crystalline precipitate phases $M_{23}C_6$ (M=Cr, W, Mo, Fe) in Ni-based superalloys. Mater Res Express 2019;6(11):116323. https://doi.org/10.1088/2053-1591/ab4fb8.